Volume 149
Number 15
7 August 2024
Pages 3873-4084

Analyst

rsc.li/analyst

ISSN 0003-2654

ROYAL SOCIETY OF CHEMISTRY

PAPER

William B. Veloso, Thiago R. L. C. Paixão *et al.*
Gold film deposition by infrared laser photothermal treatment on 3D-printed electrodes: electrochemical performance enhancement and application

Analyst

PAPER

View Article Online
View Journal | View Issue

Cite this: *Analyst*, 2024, **149**, 3900

Gold film deposition by infrared laser photothermal treatment on 3D-printed electrodes: electrochemical performance enhancement and application†

William B. Veloso, *[a] Gabriel N. Meloni, [a] Iana V. S. Arantes, [a] Lauro A. Pradela-Filho, [a] Rodrigo A. A. Muñoz [b] and Thiago R. L. C. Paixão *[a]

3D printing has attracted the interest of researchers due to its creative freedom, low cost, and ease of operation. Because of these features, this technology has produced different types of electroanalytical platforms. Despite their popularity, the thermoplastic composites used for electrode fabrication typically have high electrical resistance, resulting in devices with poor electrochemical performance. Herein, we propose a new strategy to improve the electrochemical performance of 3D-printed electrodes and to gain chemical selectivity towards glucose detection. The approach involves synthesising a nanostructured gold film using an infrared laser source directly on the surface of low-contact resistance 3D-printed electrodes. The laser parameters, such as power, focal distance, and beam scan rate, were carefully optimised for the modification steps. Scanning electronic microscopy and energy-dispersive X-ray spectroscopy confirmed the morphology and composition of the nanostructured gold film. After modification, the resulting electrodes were able to selectively detect glucose, encouraging their use for sensing applications. When compared with a gold disc electrode, the gold-modified 3D-printed electrode provided a 44-fold current increase for glucose oxidation. As proof of concept, the devices were utilised for the non-enzymatic catalytic determination of glucose in drink samples, demonstrating the gold film's catalytic nature and confirming the analytical applicability with more precise results than commercial glucometers.

Received 10th May 2024,
Accepted 17th June 2024

DOI: 10.1039/d4an00669k

rsc.li/analyst

1. Introduction

Additive manufacturing, or three-dimensional (3D) printing, is a popular technology in industrial and academic areas due to its fast ability to produce complex structures combined with accessible and inexpensive machinery and materials.[1,2] The printing process involves a layer-by-layer deposition of material over a printing platform to construct the desired part's design.[3] The most common 3D printing techniques include Fusion Deposition Modelling (FDM) and Stereolithography (SLA).[4] SLA printing consists of polymerising a light-sensitive liquid resin using UV radiation. FDM involves the extrusion of a thermoplastic filament by a heated moving nozzle.[5] SLA typically produces insulating parts, while FDM can be used to create conductive pieces due to the availability of commercial conductive filaments.[4] The resin or filament solidifies in both processes, generating the desired structure. These techniques can be used individually or combined for device fabrication, generating new sensing platforms.[6–8]

3D-printed electrodes often possess slow electron transfer kinetics and high contact resistance, affecting their electrochemical performance.[9] The latter is directly associated with the poor electrical conductivity of commercial filaments since the ratio between the conductive material and thermoplastic (electrical insulator) ranges from 10 to 20 wt%.[10] Filaments with higher amounts of conductive material can overcome this issue, but the fabrication processes of custom-made filaments are time-consuming as they involve many steps. In addition, higher carbon percentages make the filament brittle, increasing the susceptibility to clogging issues on longer prints. This limits the printer's capacity to produce devices with complex geometries, restricting them to rectangles and circles.[11,12] A simpler way to overcome contact resistance is to design electrodes with tailored geometry to reduce this ohmic drop loss.[9,13]

Post-printing surface treatments can increase the electron transfer kinetics. These methods usually involve chemical and/

[a]*Institute of Chemistry, Department of Fundamental Chemistry, University of São Paulo, 05508-000, São Paulo, SP, Brazil.*
E-mail: william.veloso@usp.br, trlcp@iq.usp.br
[b]*Institute of Chemistry, Federal University of Uberlândia, 38400-902, Uberlândia, MG, Brazil*

† Electronic supplementary information (ESI) available. See DOI: https://doi.org/10.1039/d4an00669k

or electrochemical procedures to remove the insulating thermoplastic from the electrode surface, exposing more conductive sites to the solution.[14,15] Laser ablation[16] and surface modification[17] have also been studied as alternative strategies for surface treatment. Modifying the electrode surface with metallic films promotes higher electron transfer kinetics, and it can also lead to the selective sensing of chemical species in solution if the surface chemistry is explored, such as the oxidation of glucose, which is mediated by gold oxide in alkaline solutions.[18] This can be done using an infrared (IR) laser to photothermally reduce metal ions on the electrode's surface, producing nanostructured film.[16,19] Arantes *et al.* used this approach to form gold nanostructures onto disposable paper-based electrodes for sensing applications.[20] Similarly, Scroccarello *et al.* used an IR-laser to reduce graphene oxide films, forming conductive reduced graphene oxide electrodes.[19]

Herein, we propose the fabrication of a nanostructured gold film directly on 3D-printed electrodes surface using IR-laser photothermal treatment and its application for selective glucose sensing. The electrodes were fabricated by combining FDM and masked stereolithography (MSLA) 3D printing technologies to create a geometry that minimises contact resistance. The gold modifying film was characterised by scanning electron microscopy and energy-dispersive X-ray spectroscopy, confirming the gold film formation. The electrodes were employed to quantify the glucose content in rehydration drinks, confirming their potential for selective glucose sensing.

2. Experimental section

2.1. Chemicals, materials, and samples

All chemicals were of analytical grade and used as received. Stock solutions were prepared using high-purity deionized water from a Direct-Q® 5 Ultrapure Water Systems (Millipore, MA, USA). Potassium ferrocyanide ($K_4[Fe(CN)_6]$, 99%), potassium ferricyanide ($K_3[Fe(CN)_6]$, 99%), potassium chloride (KCl, ≥99.5%), potassium hydroxide (KOH, ≥99%), sodium nitrite ($NaNO_2$, 99%), sodium sulphite (Na_2SO_3, 99%), sulfuric acid (H_2SO_4, 99%), ethyl alcohol (C_2H_6O, 99.9%) were purchased from Merk (Darmstadt, Germany). Hexaammineruthenium(III) chloride ($[Ru(NH_3)_6]Cl_3$, 99.9%), glucose (Glu, 99.9%), ascorbic acid (AA, ≥99%), citric acid (CA, 99.5%), sucrose (Suc, 99.9%) and maltose (Mal, ≥99%) were purchased from Sigma-Aldrich Co. (St Louis, MO, USA).

Carbon black/polylactic acid (CB/PLA) conductive filament was purchased from ProtoPasta (WA, USA), ABS-like resin from Elogoo (China), and M3 hex key metal screws from Lutec (SP, Brazil); these materials were used in the manufacturing of the electrodes, which will be described below. Five rehydration drink samples were purchased from a local pharmacy. Three samples were acquired in solution form and diluted in the supporting electrolyte (KOH) to the desired concentration, based on the glucose concentration described on the label (6.0 g per 500 mL, 10.0 g per 500 mL, and 11.2 g per 500 mL). Two samples were purchased in powder form, dissolved in deionized water, and then diluted in the supporting electrolyte (KOH), considering the glucose concentration described in the label (10.0 g per 500 mL and 12.0 g per 500 mL).

2.2. Apparatus

Electrochemical measurements, including cyclic voltammetry (CV), linear sweep voltammetry (LSV), and electrochemical impedance spectroscopy (EIS), were performed using an Autolab PGSTAT128N potentiostat/galvanostat with the FRA 2 module (Eco Chemie, Utrecht, The Netherlands) controlled with the NOVA 2.1.7 software. Surface modification with an IR-laser was conducted in a cutting/engraving CO_2 laser system (WorkSpecial 9060C, São Paulo, Brazil), controlled with the RD Works software (WorkSpecial, version 8.1.49). The working, counter, and reference electrodes were 3D-printed CB/PLA, platinum wire, and $Ag/AgCl/KCl_{sat}$, respectively. The 3D-printed working electrode parts were printed using an Adventurer 4 (FlashForge, 3D Technology, China) FDM 3D printer and a Mars 3 (Elegoo, China) MSLA 3D printer. A commercial gold disc electrode (diameter 3 mm) was used for comparison with the proposed electrode. The surface morphology of the electrodes was characterized using scanning electron microscopy (SEM – JEOL JSM-7401F). Elemental analysis was carried out by energy-dispersive X-ray spectroscopy (EDS). A commercial glucometer (FreeStyle Optium Neo, Abbott Laboratories, USA) was used to measure the glucose concentration in the diluted samples.

2.3. Fabrication of 3D-printed electrodes

The 3D-printed electrodes consisted of three parts, namely: the CB/PLA electrodic surface, an electric contact (M3 screw), and an insulating case serving as electrode housing, as shown in detail in Fig. S1.† The CB/PLA part consists of a 3 mm radius cylinder printed with a commercial filament (Fig. 1A). This cylinder was printed with a 3 mm diameter hole in the side face, used to insert the M3 screw, which serves as the electrical connection with the potentiostat. The working electrode area was defined by the electrode housing, consisting of a casing printed with MSLA 3D printer using an ABS-based resin. The printing parameters for the CB/PLA part and electrode housing were based on previous work,[9] and are described in the ESI.†

2.4. Modification of 3D-printed electrodes with gold using an IR-laser

The nanostructured gold film was formed directly on the surface of the CB/PLA 3D-printed electrode using an IR-laser, as shown in Fig. 1. This was made using a cutting/engraving CO_2 laser machine (WorkSpecial 9060C, São Paulo, Brazil) with a 10.6 μm wavelength, a maximum power of 40 W, and a pulse duration of 14 μs. The region scanned by the laser is a 6.0 mm diameter circle covering the upper face of the conductive cylinder, as illustrated in Fig. S1,† which corresponds to the working electrode. The parameters related to the laser

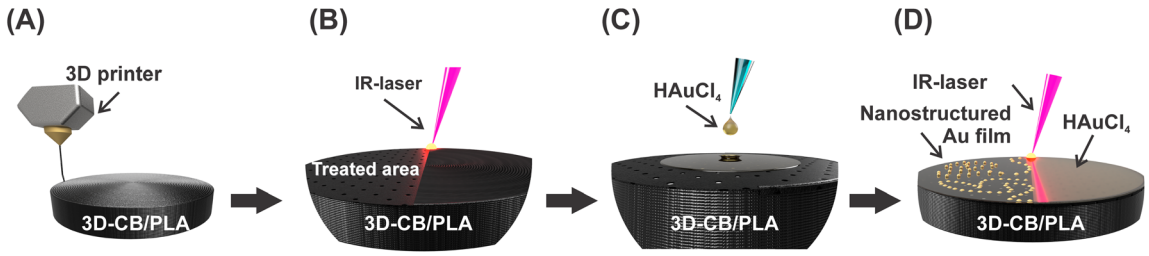

Fig. 1 Scheme of the 3D-printed electrode fabrication and modification steps: (A) printing, (B) IR-laser ablation, (C) drop-casting, and (D) IR-laser modification of 3D-CB/PLA.

beam, such as laser power (W), focal distance (mm), and beam scanning rate (mm s^{-1}), were optimized for each stage of fabrication. The working electrode was first subjected to a pre-treatment step, where the surface was ablated by the IR-laser using a laser power of 1.6 W, 7 mm focal distance, and a 20 mm s^{-1} beam scan rate (Fig. 1B), removing part of the insulating material, exposing more conductive sites to the solution, and making the surface more hydrophilic, helping in the next modification step. Subsequently, 10 μL of a 30 mmol L^{-1} $HAuCl_4$ solution (prepared in 0.5 mol L^{-1} H_2SO_4/ethanol 1 : 1) were drop-casted onto the WE surface (Fig. 1C). The drop-casting procedure was performed in two steps of 5 μL, after which the electrode was left to dry under an IR light for 10 minutes. The IR-laser beam was then scanned over the electrode surface, promoting the reduction of Au^{3+} to metallic gold (Fig. 1D). This step was conducted at 1.0 W of laser power, 9 mm focal distance and 3 mm s^{-1} beam scan rate. Hereto, the following nomenclatures will be used when referring to the as-printed electrode, ablated by IR-laser, and modified with gold nanostructured film *via* IR-laser irradiation: 3D-CB/PLA, treated 3D-CB/PLA, and modified 3D-CB/PLA, respectively.

3. Results and discussion

3.1. IR-laser parameters influence

The surface electrical resistances were used to gauge the effectiveness of the ablation step in removing the insulating PLA material from the electrode surface.[21,22] The measurement procedure is described in detail in the ESI,† and the findings are summarised in Fig. 2. Among all the parameters, laser power bears the most significant influence on surface resistance, with a minimal value of around 1.6 W, which is almost unchanged for increased laser powers (Fig. 2A). The resistance value reached a maximum when a focal distance equal to the laser lens focal distance (11 mm) was used, decreasing for lower and higher values (Fig. 2B). The laser scan rate had minimal impact on the measured resistance in the range studied (Fig. 2C). However, a slight increase is seen at 30 mm s^{-1}, indicating that with a higher scan rate, the overall dissipated power over the surface cannot effectively remove the PLA from the electrode surface. Considering the resistance values, a condition of 1.6 W laser power, 7 mm focal distance, and 20 mm s^{-1} beam scan rate was selected for this laser treatment step. At this condition, the surface resistance decreased from (1320 ± 120) Ω for the 3D-CB/PLA electrode to (273 ± 3.6) Ω for the treated 3D-CB/PLA, consistent with the improvement previously reported for 3D-printed electrodes.[16,23] This step also improved the wettability of the electrode surface, favouring the adhesion of the precursor gold solution.

The gold modification process was carried out by drop-casting 10 μL of $HAuCl_4$ solution onto the pre-treated electrode surface, followed by additional IR-laser exposure to reduce the metal ions. The laser parameters for gold reduction were evaluated considering the voltammetric profile of the modified resulting electrode using $[Fe(CN)_6]^{3-/4-}$ as a redox probe. The

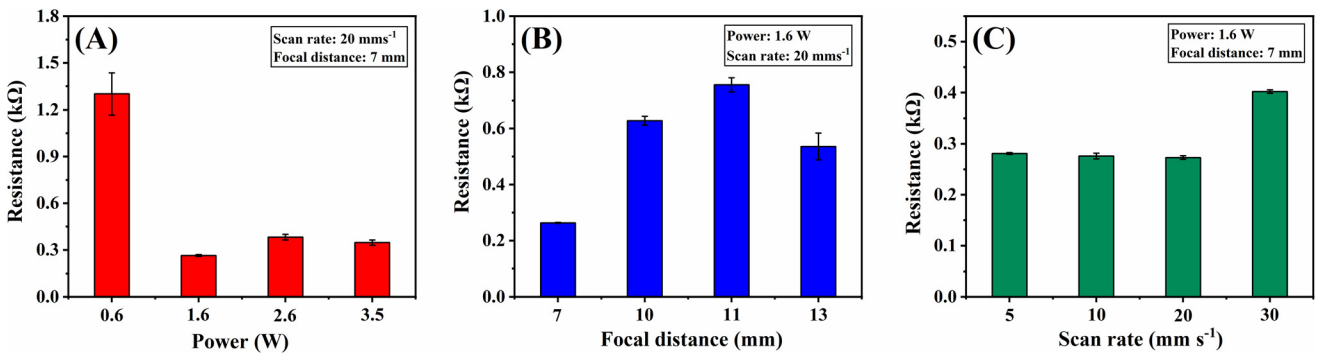

Fig. 2 Effect of IR-laser parameters variation on the electrical resistance of treated 3D-CB/PLA electrodes: (A) IR-laser power (W), (B) focal distance (mm), and (C) beam scan rate (mm s^{-1}).

changed parameters include laser power, focal distance, and beam scan rate. In the studied range, it was observed that higher laser powers improved the reversibility of the voltammetric profile. This was evidenced by an increase in peak current (I_p) values and a decrease in peak-to-peak separation (ΔE_p) (Fig. S3†). These changes suggest that the electron transfer kinetics at the surface were enhanced due to the presence of metallic gold.[24] Similar ΔE_p values are recorded for 0.6 W and 1.0 W, indicating that the gold film fully covered the electrode surface under these conditions, supported by the peak current, which is near the expected for a 6 mm flat disk (the electrode geometry), using Randles–Sevcik equation (148.7 μA).[25] At 1.0 W, the lowest ΔE_p deviation is seen, so this value was adopted for the electrode modification. Above 1.0 W, the electrode surface starts to become ablated, similar to what is seen in the first treatment step. The focal distance was studied between 7 and 13 mm (Fig. S4†), with 9 mm resulting in higher I_p and smaller ΔE_p values. Laser scan rate bears little influence on the electrochemical response (Fig. S5†), and 3 mm s^{-1} was selected as a compromise between the marginal increase in I_p and modification time.

After studying the IR-laser parameters, the volume (Fig. S6†) and concentration (Fig. S7†) of the $HAuCl_4$ solution were also optimized in this study. ΔE_p was practically the same regardless of the solution volume. However, increasing the drop-casting volume from 5 to 10 μL increased I_p to a maximum value that remained constant for volumes greater than 10 μL. This indicates that 10 μL is enough to cover the entire electrode surface with a gold film. Consequently, 10 μL was chosen for electrode modification. A 30 mmol L^{-1} $HAuCl_4$ solution concentration was selected for electrode modification since this value presented lower ΔE_p and higher I_p values. Table 1 summarizes the conditions evaluated for the modification process.

Table 1 Study of parameters for the fabrication of modified 3D-CB/PLA

Step	Parameters	Range	Selected value
Surface pre-treatment	Power (W)	0.6–3.5	1.6
	Focal distance (mm)	7–13	7
	Beam scan rate (mm s^{-1})	5–30	20
Gold reduction	Power (W)	0.3–1.0	1.0
	Focal distance (mm)	7–13	9
	Beam scan rate (mm s^{-1})	1–10	3
Drop-casting	Volume (μL)	5–20	10
	Concentration (mmol L^{-1})	5–40	30

3.2. Surface characterisation of 3D-printed electrodes

The surface morphology of 3D-printed electrodes was characterised by SEM after each fabrication step. Fig. 3A shows the 3D-CB/PLA electrodes without surface modification, just after polishing with sandpaper. Fig. 3B shows the surface after the first laser treatment, where the laser scan lines are clearly visible. After the IR-laser reduces the gold, the surface is effectively covered with a gold film (Fig. 3C). Moreover, Fig. 3D shows the presence of spherical structures of various diameters, some of them in the order of nanometres.

EDS elemental mapping analyses were conducted to investigate the composition of the electrode surface after the gold modification. Fig. 4 shows the SEM image of the edge of a modified (with gold) and unmodified region of the electrode (Fig. 4A), and corresponding elemental maps for gold (Fig. 4B), carbon (Fig. 4C), and oxygen (Fig. 4D). Fig. 4B shows

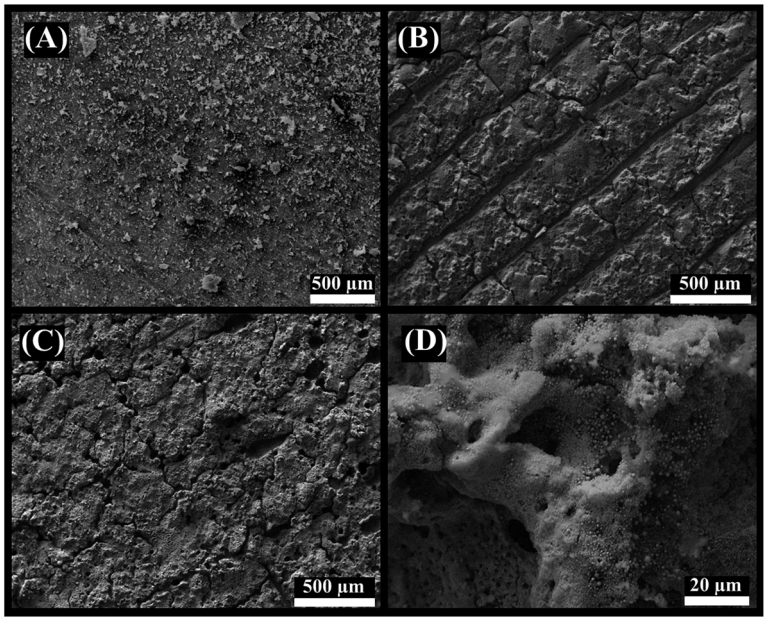

Fig. 3 SEM images of (A) 3D-CB/PLA, (B) treated 3D-CB/PLA, and (C and D) modified 3D-CB/PLA electrodes.

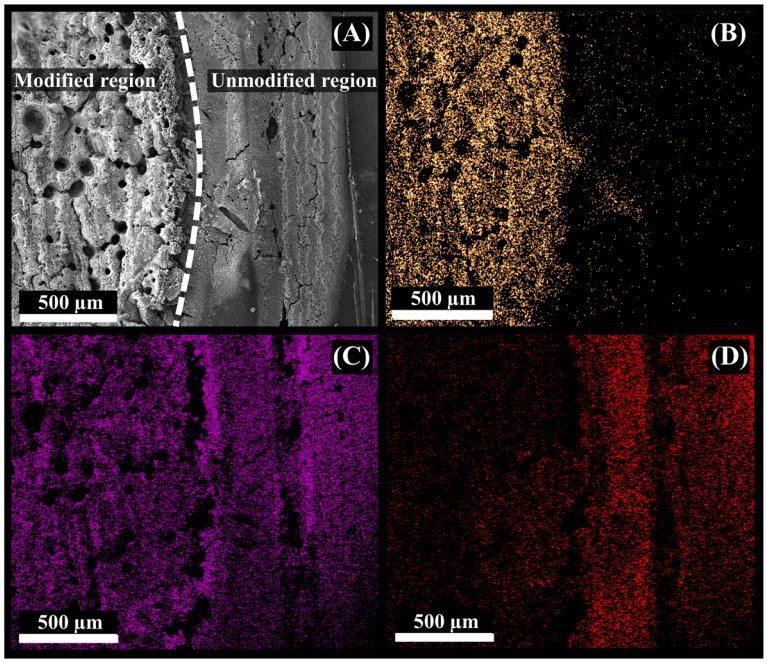

Fig. 4 (A) SEM micrograph of the modified 3D-CB/PLA electrode and colour elemental mapping images of (B) gold, (C) carbon, and (D) oxygen.

that gold is only present in the area where the IR-laser was used to reduce the gold ion, forming a metallic gold film. A clear contrast between the modified and unmodified regions is visible. Carbon and oxygen are distributed in the entire region (Fig. 4C and D), as they are present in large quantities in the PLA conductive filament, either as part of the polymer or, in the case of carbon, as carbon black, although the oxygen signal is slightly shielded by the gold layer.[26] The EDS spectra (Fig. S8†) confirmed the presence of each element and their respective weight percentage.

3.3. Electrochemical behaviour of the deposited film

The electrochemical behaviour was evaluated after each fabrication step using CV and EIS. This was initially investigated by comparing the voltammetric profile of the unmodified and modified electrodes in aqueous 0.5 mol L^{-1} H_2SO_4 solution (Fig. 5A). Modified 3D-CB/PLA electrode (red trace) provided a voltammetric profile characteristic of gold electrodes in this media. Anodic peaks observed from +0.8 V (*vs.* $Ag/AgCl/KCl_{sat}$) are associated with the oxidation of the gold surface. The presence of multiple peaks at $E > +1.0$ V indicates the formation of multiple crystallographic faces.[27,28] As expected, no faradaic process at this potential window was observed for the unmodified surface (blue trace), with the exception of solvent breakdown at the most anodic potential.

The voltammetric profiles of 3D-CB/PLA, treated 3D-CB/PLA, and modified 3D-CB/PLA electrodes were also compared using two redox probes, $[Ru(NH_3)_6]^{3+}$ and $[Fe(CN)_6]^{3-/4-}$. Fig. 5B shows the voltammograms recorded with $[Ru(NH_3)_6]^{3+}$, a surface insensitive redox probe.[29] After each fabrication step, there is a significant increase in the surface area of the electrode, evident by the larger capacitive contribution on the entire potential window, better seen in Fig. S9.† Comparing the capacitive current for the 3D-CB/PLA and modified 3D-CB/PLA electrode the surface area increased by 1544 times after the electrode treatment and modification.[30] Regardless, the peak current values for all electrodes are very similar after the capacitive current is subtracted (Table 2), expected as the surface area does not affect the faradaic currents for a reversible electrochemical process.[31] For $[Fe(CN)_6]^{3-/4-}$, the voltammetric profile of the 3D-CB/PLA electrode shows no discernible faradaic processes (Fig. 5C). Ferri/ferrocyanide is an inner sphere redox probe, *i.e.*, surface sensitive, and the absence of a well-defined faradaic process might be caused by the electrode surface charge, which is negative for the pH used (polylactic acid $pK_a \sim 3.8$).[32] Faradaic processes are seen for $[Fe(CN)_6]^{3-/4-}$ after surface treatment with the IR-laser, which increases in intensity after modification with gold thanks to the rapid electron transfer provided by the metal. All I_p and ΔE_p values are summarized in Table 2. Next, the batch-to-batch reproducibility was evaluated by comparing the electrochemical response of twelve different modified electrodes in the presence of 5.0 mmol L^{-1} $[Fe(CN)_6]^{3-/4-}$ (Fig. 5D), which indicates that the fabrication/modification process is reproducible (RSD $\leq$ 5.8% for I_p and RSD $\leq$ 4.2% for ΔE_p).

Fig. S10† displays the results obtained from the EIS analysis conducted for each step of the electrode preparation process. A typical Nyquist plot was obtained for each of the analyses. The semi-circle obtained in the high-frequency region corresponds to the charge transfer resistance (R_{ct}), and the values were calculated based on the equivalent Randles circuit (inserted in Fig. S10†). 3D-CB/PLA electrode showed a high R_{ct} value (1.45

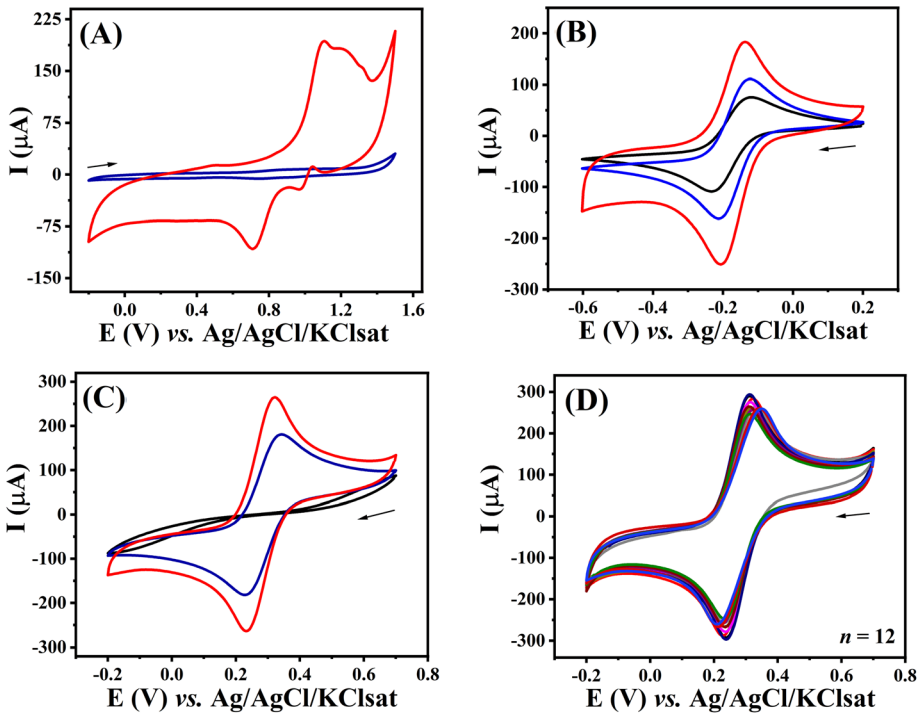

Fig. 5 CV curves of 3D-CB/PLA (black trace), treated 3D-CB/PLA (blue trace), and modified 3D-CB/PLA (red trace) in (A) 0.5 mol L^{-1} H_2SO_4, 1.0 mol L^{-1} KCl containing (B) 5.0 mmol L^{-1} $[Ru(NH_3)_6]^{3+}$, and (C) 5.0 mmol L^{-1} $[Fe(CN)_6]^{3-/4-}$. (D) Reproducibility study of modified 3D-CB/PLA in 1.0 mol L^{-1} KCl containing 5.0 mmol L^{-1} $[Fe(CN)_6]^{3-/4-}$ using 12 different electrodes; scan rate = 20 mV s^{-1}. The curves correspond to the average of three measurements (n = 3).

Table 2 Anodic peak current (I_{pa}), cathodic peak current (I_{pc}) and ΔE_p obtained with different redox probes and electrodes. Data extracted from Fig. 5B and C subtracted from capacitive currents (n = 3)

	$[Ru(NH_3)_6]^{3+}$			$[Fe(CN)_6]^{3-/4-}$		
Electrode	I_{pa} (μA)	I_{pc} (μA)	ΔE_p (mV)	I_{pa} (μA)	I_{pc} (μA)	ΔE_p (mV)
3D-CB/PLA	(85.1 ± 2.5)	(−117.1 ± 2.3)	(104 ± 5.0)	(60.5 ± 6.0)	(−67.0 ± 6.2)	650 ± 101
Treated 3D-CB/PLA	(126.2 ± 6.3)	(−136.9 ± 6.0)	(95 ± 2.6)	(167.5 ± 3.3)	(−175.9 ± 3.8)	104 ± 4.3
Modified 3D-CB/PLA	(128.6 ± 6.2)	(−139.3 ± 5.8)	(95 ± 3.2)	(241.4 ± 7.4)	(−238.3 ± 7.4)	82 ± 1.0

kΩ). This value was significantly reduced to 74.2 Ω after IR-laser treatment. R_{ct} values decreased even further after surface modification with gold *via* IR-laser irradiation (1.82 Ω). This enhancement in R_{ct} values is attributed to the gold nanostructures' higher electron transfer kinetics. These results are consistent with the cyclic voltammetry's characterizations, particularly the decrease in ΔE_p values, confirming the proposed approach's successful preparation of the modified 3D-CB/PLA electrode.

3.4. Electrooxidation of glucose at the modified 3D-CB/PLA electrode

The catalytic activity of gold electrodes towards the oxidation of glucose has been explored,[33,34] and this approach has been widely used to develop electrocatalytic platforms for non-enzymatic glucose detection.[35–38] As this is a surface-limited process, relying on the reaction of gold oxides with glucose,[39] we compared our electrode, which has a high surface area (see above), to a commercial gold disk electrode for the voltammetric response of glucose (Fig. 6A). In the absence of glucose, the modified 3D-CB/PLA electrode displayed an oxidation peak at +0.15 V *vs.* $Ag/AgCl/KCl_{sat}$ (dashed red trace). This peak corresponds to the formation of gold hydroxide and oxide species.[40] A reduction peak is observed at around +0.06 V on the reverse scan, corresponding to the reduction of the gold oxide species. After adding 10 mmol L^{-1} glucose (solid red trace), a couple of anodic peaks were observed in the forward scan. These peaks correspond to the oxidation of the gold surface and possibly of glucose or some of its intermediates.[18,41] In the reverse scan, an oxidation peak at +0.045 V is seen, corresponding to glucose oxidation by the partially reduced gold oxide in the electrode surface formed in the forward scan.[18] Compared to the flat commercial gold disc electrode (blue trace), the nanostructured gold electrode (red

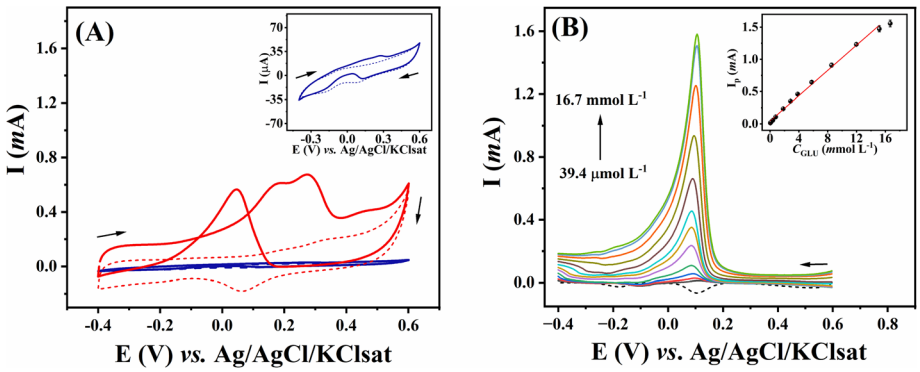

Fig. 6 (A) CV curves of a commercial gold disc electrode (blue trace) and modified 3D-CB/PLA (red trace) electrode recorded in 0.5 mol L^{-1} KOH in the absence (dashed trace) and in the presence (solid trace) of 10 mmol L^{-1} glucose. Inset: highlight the CV curve of the flat gold electrode. (B) LSV measurements for modified 3D-CB/PLA electrodes were recorded with different glucose concentrations in 0.5 mol L^{-1} KOH. Inset: peak current *vs.* glucose concentrations. Scan rate = 50 mV s^{-1}. The curves correspond to the average of three measurements (n = 3).

trace) shows a more pronounced glucose oxidation peak, expected due to the larger surface area and the fact that this mechanism of glucose oxidation is surface-limited.

The analytical performance of the proposed electrode was demonstrated by constructing a calibration curve for glucose using LSV. Peak current corresponding to glucose oxidation increased linearly with the glucose concentration from 39.4 μmol L^{-1} to 15.2 mmol L^{-1} (Fig. 6B), according to the equation: I_p(mA) = 0.098 (±0.002) C_{Glu} (mmol L^{-1}) + 0.043 (±0.014); R^2 = 0.996. This linear range is suitable for numerous glucose-sensing applications since glucose concentration in biological samples and beverages is around 5.0 mmol L^{-1}.[42] Limit of detection (LOD) and limit of quantification (LOQ) were 10.6 and 35.0 μmol L^{-1}, respectively. These were calculated as LOD = 3σ/m and LOQ = 10σ/m, where m represents the slope of the calibration plot and σ is the standard deviation obtained from ten measurements of the blank signal. Table 3 compares the analytical performance of the modified 3D-CB/PLA sensor with other electrochemical nanostructured gold sensors for non-enzymatic glucose quantification. A compatible linear range was obtained with the proposed electrode. The proposed electrode also presented LOD values that were in line with other studies, and most important, well within the glucose concentration range in biological and food samples.[42] It should be noted that the detection of glucose intermediated by gold surfaces is dependent on the electrode surface area, rather than geometric area as this is a surface-controlled phenomena. Something which is favoured in our electrode due to the large electrode size (6 mm disk) and the highly porous surface left by the treatment and fabrication steps.

Table 3 Analytical performance of sensors based on gold nanostructures previously reported for non-enzymatic glucose sensing

Electrode	Detection	Linear range (mmol L^{-1})	LOD (μmol L^{-1})	Ref.
AuNPs-PAuWEs	LSV	0.01–5.0	6.0	43
LSGE/AuNP	LSV	0.01–10.0	6.3	40
$AuNP_{HEPES}$	AMP	0.2–110	100	44
GCE/TiO_2NW/PAPBA-AuTNC	DPV	0.5–11.0	9.3	45
Au-TiO_2NTs	CV	0.05–3.0	50	46
N-GR-CNTs/AuNPs	AMP	0.002–19.6	0.5	47
AuNPs-MWCNTs-CS	AMP	0.001–1.0	0.5	42
D-gel@AuNPs	CV	0.1–30.0	67	48
AuNPs/Ni$(OH)_2$NS	AMP	0.002–6.0	0.66	49
3DG/PB-AuNPs/PDA-AuNPs/MPBA	DPV	0.005–0.065	1.5	50
GCE-GNP/GNF	CV	0.5–9.0	55	51
Modified 3D-CB/PLA	LSV	0.039–15.2	10.6	This work

AuNPs-PAuWEs: paper-based gold-sputtered working electrode modified with gold nanoparticles; LSGE/AuNP: laser-scribed graphene electrode modified with gold nanoparticles; $AuNP_{HEPES}$: gold nanoparticles prepared with 2-[4-(2-hydroxyethyl)piperazin-1-yl]ethanesulfonic acid; AMP: amperometry; GCE/TiO_2NW/PAPBA–AuTNC: glassy carbon electrode modified with a new ternary nanocomposite comprised of titanium dioxide nanowire, poly(3-aminophenyl boronic acid) and gold nanoparticles; Au-TiO_2NTs: titanium dioxide nanotubes covered with gold layers; N-GR-CNTs/AuNPs: nitrogen-doped graphene-carbon nanotubes attaching with gold nanoparticles; AuNPs-MWCNTs-CS: chitosan cryogel with embedded gold nanoparticles decorated multiwalled carbon nanotubes; AuNPs-TiO_2/PANI: gold nanoparticles and titanium dioxide modified polyaniline composite; D-gel@AuNPs: gold nanoparticles embedded D-sorbitol hydrogel; AuNPs/Ni$(OH)_2$NS: gold nanoparticles/nickel hydroxide nanosheet; 3DG/PB-AuNPs/PDA-AuNPs/MPBA: 3D graphene/Prussian blue/gold nanoparticles/polydopamine/mercaptobenzoboric acid; DPV: differential pulse voltammetry; GCE-GNP/GNF: glassy carbon electrode decorated with gold nanoparticles incorporated graphene nanofibers.

3.5. Selectivity study

The analytical response for glucose of the proposed electrode was studied in the presence of coexisting species commonly found with glucose in food samples. The tests were performed by recording LSV measurements in the presence of 1 mmol L^{-1} glucose and potential interfering species at ratios of 10 : 1 and 2 : 1. They include ascorbic acid, citric acid, nitrite and sulphite, and the carbohydrates sucrose and maltose. Peak current variations of more than 10% were considered interfering.[52] No significant change was observed in the presence of

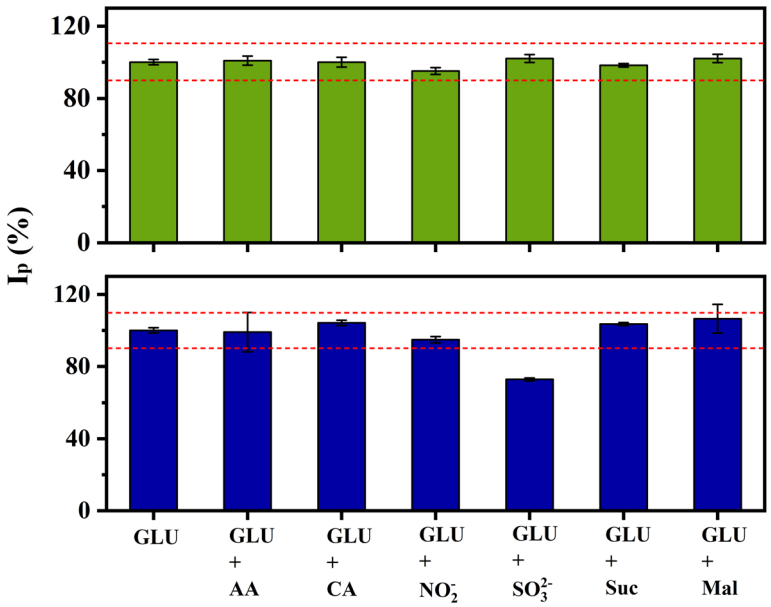

Fig. 7 Interference study performed by LSV with 1.0 mmol L^{-1} glucose (Glu) in the presence of 0.1 mmol L^{-1} (green bars) and 0.5 mmol L^{-1} (blue bars) of ascorbic acid (AA), citric acid (CA), nitrite (NO_2^-), sulphite (SO_3^{2-}), sucrose (Suc) and maltose (Mal). The values correspond to the average of three measurements (n = 3).

0.1 mmol L^{-1} (10 : 1 ratio) of all components (Fig. 7). When the interferents were at a concentration of 0.5 mmol L^{-1}, only sulphite interfered in the measurements, decreasing the current by 30%. This behaviour is likely due to the strong affinity between gold and species containing sulphur,[53,54] partially blocking the electrode surface. The interference of sulphite can be dealt by pre-treating the sample, converting sulphite to $SO_{2(g)}$,[55] or oxidized to SO_4^{2-}.[56]

3.6. Drink sample analysis

The practical applicability of the modified 3D-CB/PLA sensor was next evaluated by analysing the glucose content in commercial rehydration drinks, including solution and powder. After solubilizing the powder in deionised water, all the samples were diluted in supporting electrolyte to reach a concentration within the linear range based on the labelled glucose concentration. The real glucose concentration was calculated using the analytical curve (Fig. 6B). The reliability of the sensor was evaluated by comparing the results obtained with a commercial glucometer. Table 4 shows that the proposed sensor provided results comparable to the conventional glucometer, with measurement errors within 5% of each other for all samples (relative error, Table 4). It is worth noting that the measurements with the modified 3D-CB/PLA electrode were more precise (lower RSD) than the glucometer measurements.

Table 4 Determination of glucose in commercial samples of rehydration solution and powder for preparing rehydration solutions (n = 5[a])

Samples	Nominal concentration (g per 500mL)	Measured by modified CB/PLA (g per 500 mL)	Measured by glucometer (g per 500 mL)	Relative error[d] (%)
S_1[b]	6.00	(5.52 ± 0.1)	(5.78 ± 0.5)	4.5
S_2[b]	10.0	(11.41 ± 0.1)	(11.14 ± 0.4)	2.4
S_3[b]	11.2	(9.82 ± 0.1)	(10.31 ± 0.3)	4.7
S_4[c]	10.0	(10.10 ± 0.1)	(9.85 ± 0.5)	2.5
S_5[c]	12.0	(11.73 ± 0.2)	(11.32 ± 0.1)	3.6

[a] This result is an average of five determinations. [b] Oral rehydration solution. [c] Powder for oral rehydration solution. [d] Relative error between the proposed method and commercial glucometer.

4. Conclusion

A gold film was formed directly onto 3D-printed electrode surfaces using a photothermal treatment with IR-laser. The electrodes were produced by combining two 3D printing techniques, FDM and MSLA. After printing and assembly, the devices were subjected to a pre-treatment by an IR-laser to partially remove the insulating polymeric material from the electrode surface. Afterwards, the 3D-printed electrodes were modified with a gold nanostructured film induced by IR-laser. SEM images and elemental mapping of the electrode surface confirmed the electrode's modification and its morphological characteristics. The electrochemical performance improved due to increased electron transfer rates afforded by the gold structures anchored on the carbon surface. The electrode was employed for the non-enzymatic glucose detection. The modified 3D-CB/PLA provided a linear range from 39 μmol L^{-1} to 15.2 mmol L^{-1}, with an LOD of 10.6 μmol L^{-1}. As proof of concept, the electrodes were applied to determine glucose in

commercial beverage samples, providing results comparable with those obtained with the commercial glucometer.

Data availability

The data supporting this article have been included as part of the ESI.†

Author contributions

William B. Veloso: investigation, methodology, visualization, and writing original draft; Gabriel N. Meloni: investigation, methodology, review, and editing; Iana V. S. Arantes: methodology and data curation; Lauro A. Pradela-Filho: methodology and data curation; Rodrigo A. A. Muñoz: investigation and supervision; Thiago R. L. C. Paixão: investigation, review, funding acquisition, supervision, conceptualization, and project administration. All authors have given approval to the final version of the manuscript.

Conflicts of interest

The authors declare no conflict of interest.

Acknowledgements

The authors are also grateful to Fernando A. Fernandes and Central Analítica (IQ/USP) for the help with the SEM images and infrastructure. We also thank LABMICRO from the University of São Paulo for the SEM/EDX images. This research was supported by São Paulo Research Foundation (FAPESP) (Grant Numbers: 2019/15065-7, 2021/00205-8, 2022/11346-4, 2022/03382-0, 2021/00800-3 and 2023/00246-1), Conselho Nacional de Desenvolvimento Científico e Tecnológico (CNPq, Grant Number: 140462/2021-0 and 315838/2021-3), Coordenação de Aperfeiçoamento de Pessoal de Nível Superior (CAPES) (Finance Code 001).

References

1 M. A. Ali, C. Hu, E. A. Yttri and R. Panat, *Adv. Funct. Mater.*, 2022, **32**(9), 2107671.
2 B. M. C. Costa, A. G. Coelho, M. J. Beauchamp, J. B. Nielsen, G. P. Nordin, A. T. Woolley and J. A. F. da Silva, *Anal. Bioanal. Chem.*, 2022, **414**, 545–550.
3 H. H. Hamzah, S. A. Shafiee, A. Abdalla and B. A. Patel, *Electrochem. Commun.*, 2018, **96**, 27–31.
4 A. Ambrosi and M. Pumera, *Chem. Soc. Rev.*, 2016, **45**, 2740–2755.
5 J. J. Tully and G. N. Meloni, *Anal. Chem.*, 2020, **92**, 14853–14860.
6 F. Li, N. P. MacDonald, R. M. Guijt and M. C. Breadmore, *Anal. Chem.*, 2019, **91**, 1758–1763.
7 B. M. Brenda, S. Griveau, F. Bedioui, F. d'Orlye, J. A. F. da Silva and A. Varenne, *Electrochim. Acta*, 2022, **407**, 139888.
8 R. M. Cardoso, S. V. F. Castro, M. N. T. Silva, A. P. Lima, M. H. P. Santana, E. Nossol, R. A. B. Silva, E. M. Richter, T. R. L. C. Paixão and R. A. A. Muñoz, *Sens. Actuators, B*, 2019, **292**, 308–313.
9 W. B. Veloso, T. R. L. C. Paixão and G. N. Meloni, *Electrochim. Acta*, 2023, **449**, 142166.
10 J. S Stefano, C. Kalinke, R. G. da Rocha, D. P. Rocha, V. A. O. P. da Silva, J. A. Bonacin, L. Angnes, E. M. Richter, B. C. Janegitz and R. A. A. Muñoz, *Anal. Chem.*, 2022, **94**(17), 6417–6429.
11 J. S. Stefano, L. R. G. Silva, R. G. Rocha, L. C. Brazaca, E. M. Richter, R. A. A. Muñoz and B. C. Janegitz, *Anal. Chim. Acta*, 2022, **1191**, 339372.
12 R. G. Rocha, R. M. Cardoso, P. J. Zambiazi, S. V. F. Castro, T. V. B. Ferraz, G. de O. Aparecido, J. A. Bonacin, R. A. A. Munoz and E. M. Richter, *Anal. Chim. Acta*, 2020, **1132**, 1–9.
13 R. D. Crapnell, A. G. M. Ferrari, M. J. Whittingham, E. Sigley, N. J. Hurst, E. M. Keefe and C. E. Banks, *Sensors*, 2022, **22**(23), 9521.
14 R. Gusmão, M. P. Browne, Z. Sofer and M. Pumera, *Electrochem. Commun.*, 2019, **102**, 83–88.
15 E. M. Richter, D. P. Rocha, R. M. Cardoso, E. M. Keefe, C. W. Foster, R. A. A. Munoz and C. E. Banks, *Anal. Chem.*, 2019, **91**, 12844–12851.
16 W. B. Veloso, V. N. Ataide, D. P. Rocha, H. P. Nogueira, A. De Siervo, L. Angnes, R. A. A. Muñoz and T. R. L. C. Paixão, *Microchim. Acta*, 2023, 1–11.
17 V. Katic, P. L. Dos Santos, M. F. Dos Santos, B. M. Pires, H. C. Loureiro, A. P. Lima, J. C. M. Queiroz, R. Landers, R. A. A. Muñoz and J. A. Bonacin, *ACS Appl. Mater. Interfaces*, 2019, **11**, 35068–35078.
18 M. Pasta, F. La Mantia and Y. Cui, *Electrochim. Acta*, 2010, **55**, 5561–5568.
19 A. Scroccarello, R. Álvarez-Diduk, F. Della Pelle, C. C. C. Silva, A. Idili, C. Parolo, D. Compagnone and A. Merkoçi, *ACS Sens.*, 2023, **8**(2), 598–609.
20 I. V. S. Arantes, V. N. Ataide, W. A. Ameku, J. L. M. Gongoni, J. S. G. Selva, H. P. Nogueira, M. Bertotti and T. R. L. C. Paixão, *Sens. Diagn.*, 2023, **2**, 111–121.
21 W. R. de Araujo, C. M. R. Frasson, W. A. Ameku, J. R. Silva, L. Angnes and T. R. L. C. Paixão, *Angew. Chem.*, 2017, **129**, 15309–15313.
22 L. F. Mendes, A. de Siervo, W. R. de Araujo and T. R. L. C. Paixão, *Carbon*, 2020, **159**, 110–118.
23 D. P. Rocha, V. N. Ataide, A. de Siervo, J. M. Gonçalves, R. A. A. Muñoz, T. R. L. C. Paixão and L. Angnes, *Chem. Eng. J.*, 2021, **425**, 130594.
24 J. Velmurugan, P. Sun and M. V. Mirkin, *J. Phys. Chem. C*, 2009, **113**, 459–464.
25 J. E. B. Randles, *Trans. Faraday Soc.*, 1948, **44**, 327–338.
26 I. Proto-Pasta, *Electrically Conductive Composite PLA*, 2024.

27 H. Shu, L. Cao, G. Chang, H. He, Y. Zhang and Y. He, *Electrochim. Acta*, 2014, **132**, 524–532.
28 B. Lertanantawong, A. P. O'Mullane, W. Surareungchai, M. Somasundrum, L. D. Burke and A. M. Bond, *Langmuir*, 2008, **24**, 2856–2868.
29 P. Nayak, N. Kurra, C. Xia and H. N. Alshareef, *Adv. Electron. Mater.*, 2016, **2**, 1–11.
30 D. Voiry, M. Chhowalla, Y. Gogotsi, N. A. Kotov, Y. Li, R. M. Penner, R. E. Schaak and P. S. Weiss, *ACS Nano*, 2018, **12**, 9635–9638.
31 T. R. L. C. Paixão, *ChemElectroChem*, 2020, **7**, 3414–3415.
32 L. A. Pradela-Filho, W. B. Veloso, D. N. Medeiros, R. S. O. Lins, B. Ferreira, M. Bertotti and T. R. L. C. Paixão, *Anal. Chem.*, 2023, **95**, 10634–10643.
33 Y. B. Vassilyev, O. A. Khazova and N. N. Nikolaeva, *J. Electroanal. Chem.*, 1985, **196**, 127–144.
34 M. W. Hsiao, R. R. Adzic and E. B. Yeager, *J. Electrochem. Soc.*, 1996, **143**, 759.
35 G. X. Zhong, W. X. Zhang, Y. M. Sun, Y. Q. Wei, Y. Lei, H. P. Peng, A. L. Liu, Y. Z. Chen and X. H. Lin, *Sens. Actuators, B*, 2015, **212**, 72–77.
36 G. Chang, H. Shu, K. Ji, M. Oyama, X. Liu and Y. He, *Appl. Surf. Sci.*, 2014, **288**, 524–529.
37 D. W. Hwang, S. Lee, M. Seo and T. D. Chung, *Anal. Chim. Acta*, 2018, **1033**, 1–34.
38 K. E. Toghill and R. G. Compton, *Int. J. Electrochem. Sci.*, 2010, **5**, 1246–1301.
39 L. A. Larew and D. C. Johnson, *J. Electroanal. Chem.*, 1989, **262**, 167–182.
40 B. Zhu, L. Yu, S. Beikzadeh, S. Zhang, P. Zhang, L. Wang and J. Travas-Sejdic, *Electrochim. Acta*, 2021, **378**, 138132.
41 W. T. Chiu, T. F. M. Chang, M. Sone, A. Tixier-Mita and H. Toshiyoshi, *Talanta*, 2020, **212**, 120780.
42 T. Kangkamano, A. Numnuam, W. Limbut, P. Kanatharana and P. Thavarungkul, *Sens. Actuators, B*, 2017, **246**, 854–863.
43 E. Núnez-Bajo, M. C. Blanco-López, A. Costa-García and M. T. Fernández-Abedul, *Talanta*, 2018, **178**, 160–165.
44 S. Karra, M. Wooten, W. Griffith and W. Gorski, *Electrochim. Acta*, 2016, **218**, 8–14.
45 N. Muthuchamy, A. Gopalan and K. P. Lee, *RSC Adv.*, 2018, **8**, 2138–2147.
46 K. Grochowska, J. Ryl, J. Karczewski, G. Śliwiński, A. Cenian and K. Siuzdak, *J. Electroanal. Chem.*, 2019, **837**, 230–239.
47 H. Jeong, D. M. Nguyen, M. S. Lee, H. G. Kim, S. C. Ko and L. K. Kwac, *Mater. Sci. Eng., C*, 2018, **90**, 38–45.
48 J. Zhao, X. Hu, X. Huang, X. Jin, K. Koh and H. Chen, *Colloids Surf., B*, 2019, **183**, 110404.
49 J. Xu, T. Chen, X. Qiao, Q. Sheng, T. Yue and J. Zheng, *Colloids Surf., A*, 2019, **561**, 25–31.
50 Q. Liu, H. Zhong, M. Chen, C. Zhao, Y. Liu, F. Xi and T. Luo, *RSC Adv.*, 2020, **10**, 33739–33746.
51 A. S. Shamsabadi, H. Tavanai, M. Ranjbar, A. Farnood and M. Bazarganipour, *Mater. Today Commun.*, 2020, **24**, 100963.
52 A. Blidar, O. Hosu, B. Feier, G. Ștefan, D. Bogdan and C. Cristea, *Food Chem.*, 2022, **371**, 131127.
53 J. R. Reimers, M. J. Ford, S. M. Marcuccio, J. Ulstrup and N. S. Hush, *Nat. Rev. Chem.*, 2017, **1**(2), 0017.
54 Y. W. Yang and L. J. Fan, *Langmuir*, 2002, **18**, 1157–1164.
55 D. A. G. Araújo, A. C. M. Oliveira, L. A. Pradela-Filho, R. M. Takeuchi and A. L. Santos, *Anal. Chim. Acta*, 2021, **1185**, 339067.
56 R. F. Mcfeeters, *J. Food Prot.*, 1998, **61**, 885–890.